Astronomy & Astrophysics manuscript no. aa
March 1, 2013

The magnetic field of IRAS 16293-2422 as traced by shock-induced H_2O masers

F. O. Alves[1], W. H. T. Vlemmings[2], J. M. Girart[3] and J. M. Torrelles[4]

[1] Argelander-Institut für Astronomie, University of Bonn, Auf dem Hügel 71, D-53121 Bonn, Germany
e-mail: falves@astro.uni-bonn.de
[2] Chalmers University of Technology, Onsala Space Observatory, SE-439 92 Onsala, Sweden
e-mail: wouter.vlemmings@chalmers.se
[3] Institut de Ciències de l'Espai (IEEC–CSIC), Campus UAB, Facultat de Ciències, C5 par 2ª, 08193 Bellaterra, Catalunya, Spain
e-mail: girart@ice.cat
[4] Institut de Ciències de l'Espai (CSIC)-UB/IEEC, Universitat de Barcelona, Martí i Franquès 1, E-08028 Barcelona, Spain
e-mail: torrelles@ieec.cat

Received ; accepted

ABSTRACT

Context. Shock-induced H_2O masers are important magnetic field tracers at very high density gas. Water masers are found in both high- and low-mass star-forming regions, acting as a powerful tool to compare magnetic field morphologies in both mass regimes.
Aims. In this paper, we show one of the first magnetic field determinations in the low-mass protostellar core IRAS 16293-2422 at volume densities as high as 10^{8-10} cm^{-3}. Our goal is to discern if the collapsing regime of this source is controlled by magnetic fields or other factors like turbulence.
Methods. We used the Very Large Array (VLA) to carry out spectro-polarimetric observations in the 22 GHz Zeeman emission of H_2O masers. From the Stokes V line profile, we can estimate the magnetic field strength in the dense regions around the protostar.
Results. A blend of at least three maser features can be inferred from our relatively high spatial resolution data set ($\sim 0.1''$), which is reproduced in a clear non-Gaussian line profile. The emission is very stable in polarization fraction and position angle across the channels. The maser spots are aligned with some components of the complex outflow configuration of IRAS 16293-2422, and they are excited in zones of compressed gas produced by shocks. The post-shock particle density is in the range of $1 - 3 \times 10^9$ cm^{-3}, consistent with typical water masers pumping densities. Zeeman emission is produced by a very strong line-of-sight magnetic field ($B \sim 113$ mG)
Conclusions. The magnetic field pressure derived from our data is comparable to the ram pressure of the outflow dynamics. This indicates that the magnetic field is energetically important in the dynamical evolution of IRAS 16293-2422.

Key words. stars: formation – masers – polarization – ISM: magnetic fields – ISM: individual objects: IRAS 16293-2422

1. Introduction

Spectro-polarimetric observations of masers are a powerful tool to study the magnetic field properties in the maser pumping zone. Water masers are unique because they are found in a variety of astrophysical environments and, in particular, in star-forming regions at distinct mass regimes. In contrast, methanol and OH masers are found associated mostly with high-mass star formation sites (e.g., Vlemmings 2008; Sanna et al. 2010a,b). The most commonly observed water maser line is the $(6_{16} - 5_{23})$ transition at 22 GHz, an excellent probe of molecular gas at very high volume densities (n_{H_2} in the 10^8 to 10^{10} cm^{-3} range, Elitzur et al. 1989). While the Zeeman splitting is small ($\sim 10^{-3}$ Hz μG^{-1}), the line strength is sometimes sufficient for measuring the circular polarization and therefore for a direct measurement of the line-of-sight (LOS) component of the magnetic field. If linear polarization is also measured, then the full 3-D magnetic field configuration can be derived.

Recently, several studies have appeared in the literature reporting the efficiency of maser spectro-polarimetry technique using masers. These studies have revealed the magnetic field properties in very dense molecular environment around the circumstellar envelopes of evolved stars and young stars (e.g., Surcis et al. 2011a,b; Pérez-Sánchez et al. 2011). A representative result regarding how magnetic fields can be resolved in very small spatial scales was obtained by Vlemmings et al. (2006), who carried out Very Long Baseline Array (VLBA) polarization observations of H_2O masers around the Cepheus A HW2 high-mass object.

Thermal dust polarization emission is difficult to observe in the most embedded portions of molecular clouds due to the low sensitivity to polarized data (and the feasibility is then limited toward a handful list of objects). Submillimeter (submm) emission suffers from depolarization effects like unresolved fields or roundness of dust grains (Goodman et al. 1992, 1995; Lazarian et al. 1997). Water masers can be thought as an observational tool to overcome this issue, since they are excited at very high densities.

IRAS 16293-2422 (hereafter, I16293), is a prototypical low-mass protostellar system located in the ρ Ophiuchus molecular cloud ($d \simeq 120$ pc, Loinard et al. 2008). This source is a well-studied binary system, usually referred as source A and B, with angular separation of $5''$ (600 AU) and very embedded in a dense molecular core (Wootten 1989; Looney et al. 2000). Both sources have a very rich chemistry which is typically found in hot cores (Ceccarelli et al. 2000; Kuan et al. 2004; Bisschop et al. 2008; Jørgensen et al. 2011). Although component B appears to

be a single source, high resolution interferometer data reveal a higher degree of fragmentation for source A. In fact, two dust submm components were detected within this object with an angular separation of ~ 0.6″ (~ 72 AU, Chandler et al. 2005). I16293 has two large scale (~ 1′) bipolar CO outflows, one of them associated with source A while the powering source of the other CO outflow is a matter of debate (Walker et al. 1988; Stark et al. 2004; Yeh et al. 2008). Recently, observations of the SiO (8–7) emission have revealed a compact molecular outflow also associated with source A (Rao et al. 2009). I16293 has strong water maser emission that has been well monitored (Wilking & Claussen 1987; Terebey et al. 1992; Claussen et al. 1996; Furuya et al. 2003). The strongest features appear at blueshifted and redshifted LSR velocities with respect to the ambient cloud velocity (~ 4 km s^{-1}), typically between V_{LSR} of -5 and 10 km s^{-1}. The H_2O maser emission very often has intensities of more than 100 Jy, and at times it is stronger than 300 Jy, at LSR velocities of ~ 7 km s^{-1}.

Tamura et al. (1993) performed observations of the 1.1 mm dust polarized emission toward I16293 at an angular resolution of 19″. They found that the magnetic field lines are perpendicular to the major axis of the dense elongated disk-like molecular structure (~ 10″ size, ~ 1200 AU) observed in $C^{18}O$ by Mundy et al. (1990). This configuration was corroborated recently by Rao et al. (2009), who used the Submillimeter Array (SMA) and obtained a polarization map at an angular resolution of ~ 2″ (~ 240 AU), resolving both sources A and B. The mean volume density traced by the SMA maps is ~ 6×10^7 cm^{-3}. The polarization pattern around source A is compatible with a hourglass morphology for the magnetic field, whose strength was estimated in ~ 4.5 mG. The SMA maps show that there is a misalignment between the outflow direction and the magnetic field axis, roughly in agreement with model predictions where the magnetic energy is comparable to the centrifugal energy. In contrast, source B is associated with an uniform and apparently undisturbed magnetic field.

In this work, we report spectro-polarimetric Very Large Array (VLA) observations of H_2O masers toward I16293. In § 2, we describe the details of the observational setup. In § 3, the results obtained from the maser spectroscopy are shown. In § 4, we discuss a possible correlation between the masers features and the outflows. The magnetic field strength estimation and its implication on the core dynamical evolution are discussed in sections 5 and 6, respectively. Finally in § 7 we summarize our conclusions.

2. Observations

The observations were done with the VLA (NRAO[1], New Mexico, USA) in its extended A-configuration, on 2007 June 25$^{\text{th}}$ and 27$^{\text{th}}$. The tracks lasted ~ 5.5 hours each. A total of 27 antennas were used, 10 of them already retrofitted with the new system, resulting in a combined VLA/EVLA (Extended VLA) observation. We used the K band receivers (22-24 GHz) tuned at the frequency of the water maser ($6_{16} - 5_{23}$) rotational transition (ν_0 = 22.23508 GHz). We used the full polarization capability of the correlator, selecting a bandwidth of 0.7813 MHz (~ 10.5 km s^{-1} in velocity). The spectral setup contains a total of 128 channels which covers most of the velocity range of the strongest water maser features (observed around the brightest feature previously reported at ~ 7 km s^{-1}) at the spectral resolution of 0.08 km s^{-1}. The quasar J1626-298 was used as gain calibrator. The quasar J1331+305 and the radio source J1751+096 were used for polarization calibrations in order to obtain corrections in the instrumental feed polarization and the corrected position angle of the polarization vectors. All three calibrators were also used for bandpass corrections. We performed self–calibration using the channel with the strongest intensity. Since the detected emission is unresolved, both phase and amplitude self–calibration solutions were applied to the other channels.

The combined VLA/EVLA setup introduces about 8% closure errors on VLA-EVLA baselines-based corrections on the bandpass. This happens due to the distinct bandpass response of the EVLA antennas compared to the VLA ones. These errors become more severe at narrow bandwidths, when the processing of the digital signal of EVLA antennas aliases the power response at the band edges. During the data reduction, we took special care on determining the bandpass solutions by performing particular calibration strategies recommended to the user in the NRAO webpage[2]. They consisted of flagging EVLA-EVLA baselines prior to bandpass calibration and unflagging them prior to applying the bandpass solutions to the data set. The bandpass corrections are then applied to an averaged single-channel multi-source dataset ("channel 0" file) and to the multi-channel original file.

Data reduction was done with the Astronomical Image Processing Software package (AIPS). Imaging of Stokes parameters I, Q, and U were generated with a quasi-uniform weighting (*robust* = -1, Briggs 1995). Maps of polarized fraction (P) and position of polarization angles (PA) were obtained by combining Stokes Q and U images in such a way that $P = \frac{I_P}{I} = \frac{\sqrt{Q^2+U^2}}{I}$ and PA = $\frac{1}{2}\tan^{-1}(\frac{U}{Q})$. The resulting synthesized beam is $0.14'' \times 0.08''$, with a position angle of $-5.7°$. The rms noise for channels where no emission is detected is ~ 8 mJy beam^{-1}, and it increases up to 23 mJy beam^{-1} at the peak emission channel. A slightly lower rms is observed for polarized intensity.

3. Results

3.1. H_2O maser line

The contour channel maps of the H_2O emission observed with the VLA/EVLA data are shown in Fig. 1. The emission extends over a wide range of velocities (4.5 < V_{LSR} < 9 km s^{-1}), i. e., at redshifted LSR velocities with respect to the cloud systemic velocity (~ 4 km s^{-1}). Our spectral setup covers only a small portion of LSR velocities blueward of it (~ 2 < V_{LSR} < 4 km s^{-1}) but no emission was detected within this spectral range. The water maser line has peak intensity of 170 Jy beam^{-1}, detected at $V_{LSR} \simeq$ 7.4 km s^{-1}. This emission was extensively reported in previous surveys also as the brightest feature (see, for instance, Claussen et al. 1996; Furuya et al. 2003). Some channels have emission extended slightly eastward (V_{LSR} between $\simeq$ 6.5 and 7 km s^{-1}), suggesting that the observed emission in these channels is marginally resolved.

A scheme of the distribution of dust and molecular outflows in I16293 is shown in Fig. 2. The masers detected in our observations are associated with source A. They are located ~ 0.25″ (~ 30 AU in projection) to the southeast of the dust condensation *Aa* resolved by the subarcsecond submillimeter (submm) observations of Chandler et al. (2005).

[1] The National Radio Astronomy Observatory - NRAO - is a facility of the National Science Foundation, operated under cooperative agreement by Associated Universities, Inc.

[2] http://www.vla.nrao.edu/astro/guides/evlareturn/postproc/index.shtml#closure-line

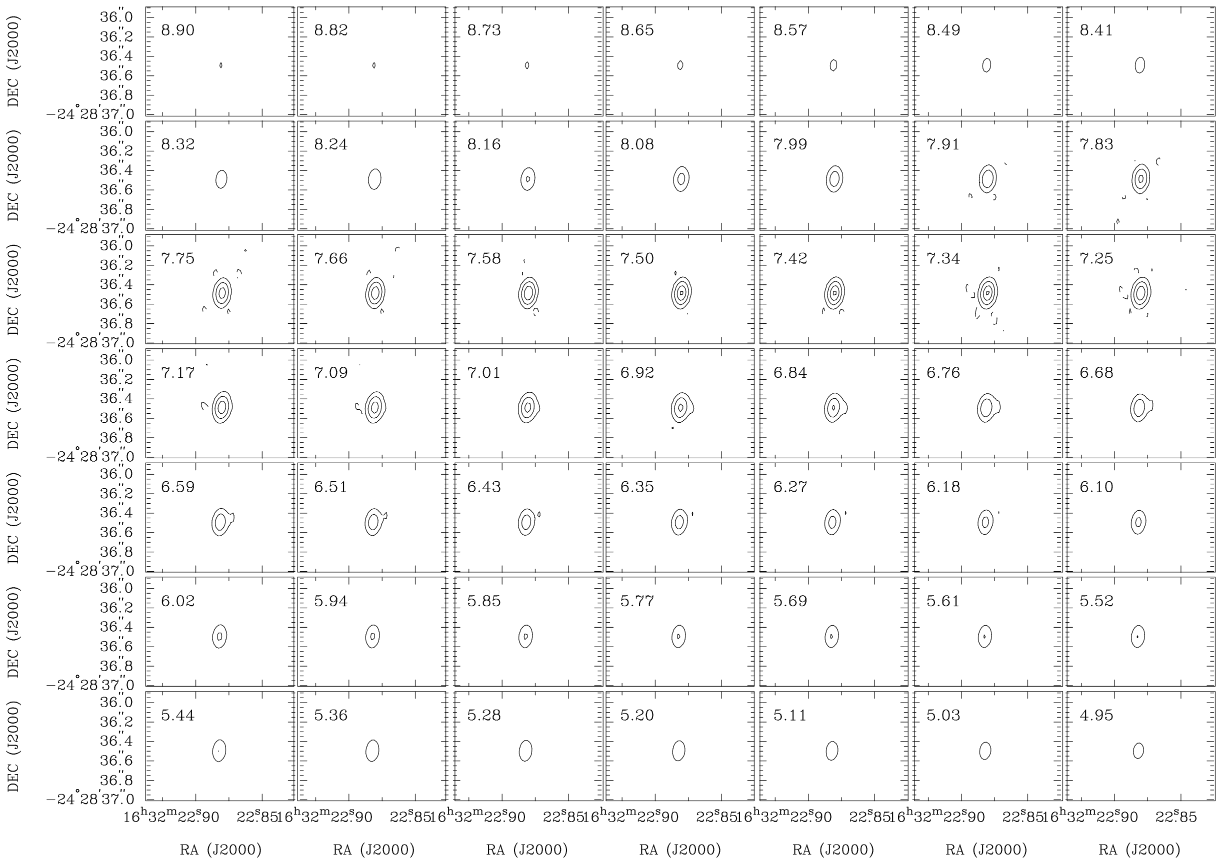

Fig. 1. Channel maps of the H_2O emission toward IRAS 16293-2422. Contours are -50, 50, 500, $3{\times}10^3$, $1{\times}10^4$, $2{\times}10^4$ times 8 mJy beam^{-1}, the rms noise of the maps with lower intensities (see Section 2). The peak flux of 167 Jy beam^{-1} occurs at V_{LSR} = 7.4 km s^{-1}. The LSR velocity of each channel is labelled.

The Stokes I spectrum of the maser emission is shown in Fig. 3 (upper panel). The non-Gaussian line profile indicates that there are unresolved components in the spectrum. Apart of the peak intensity at 7.4 km s^{-1}, unresolved emission seems to be also present at lower velocities ($V_{LSR} \simeq 5.5$ km s^{-1}) with a strong flux of $\sim$ 20 Jy beam^{-1}. Fainter emission ($\sim$ 5 Jy beam^{-1}) is also observed at higher velocity channels ($V_{LSR} \simeq 9.2$ km s^{-1}). Therefore, there are at least three unresolved components (Table 1). A two-dimensional Gaussian profile fit on each of those components provides a mean spatial separation of $\sim$ 22 milliarcseconds (mas), which is higher than the precision on the relative position determination ($rms_{pos} \simeq 2$ mas, estimated from the ratio between the width of the synthesized beam and the signal-to-noise ratio of the fainter component).

Table 1. H_2O maser components in IRAS 16293-2422

V_{LSR} (km s^{-1})	I^{a}_{peak} (Jy beam^{-1})	α (2000) (h m s)	δ (2000) (o ′ ″)
5.7	23	16 32 22.8830	-24 28 36.495
7.4	168	16 32 22.8808	-24 28 36.487
9.2	5	16 32 22.8818	-24 28 36.493

[a] Equatorial coordinates derived with the JMFIT task of AIPS.

3.2. Polarized emission

The spectrum of linearly polarized intensity is very similar to the Stokes I line profile except for the flux scale. It peaks at the same systemic velocity as the Stokes I spectrum, although it is weaker by a factor of $\sim$ 30. The dependence of the linear polarization intensity, polarization fraction, position angle and Stokes I with systematic velocity is shown in Fig. 3. The measured polarization fraction is 2.5 ± 0.2%. The polarization position angle θ is $-23°$ and shows only small changes across the maser ($\sigma_\theta = 2°$), implying that the polarization vectors at different velocities trace basically the same region. The formal uncertainty in PA ($\sigma_\theta = \frac{1}{2}\frac{\sigma_P}{I_P}\frac{180^\circ}{\pi}$, Wardle & Kronberg 1974) is small and ranges between $\sim 0.14°$ and $0.80°$ considering channels with strong and weak linear polarization emission, respectively. The linear polarization as derived from Stokes U and Q maps is exhibited in Fig. 4, which shows the distribution of polarization vectors in the brightest velocity channel. The peak of polarized intensity is offset 0.05″ with respect to the Stokes I peak. The polarization vectors can be parallel or perpendicular to magnetic field orientation in the plane of the sky. In § 5, we discuss which assumptions must be considered in order to solve this ambiguity.

The line profile of the circular polarization (Stokes V) has the characteristic S-shape (see Fig. 5, lower panel). The Stokes V spectrum is proportional to the first derivative of the Stokes I spectrum and to the LOS component of the magnetic field. The red dashed line in Fig. 5 indicates the fit which best represents this derivation. Due to remaining gain differences among the two polarizations, scaled down replicas of Stokes I spectrum might contaminate the Stokes V data (Sarma et al. 2001; Vlemmings et al. 2002). These features were considered in the fit and subtracted from the synthetic V spectrum. The fraction of circular polarization, calculated as $(V_{max} - V_{min})/I_{max}$, is $\sim$ 0.45% for the

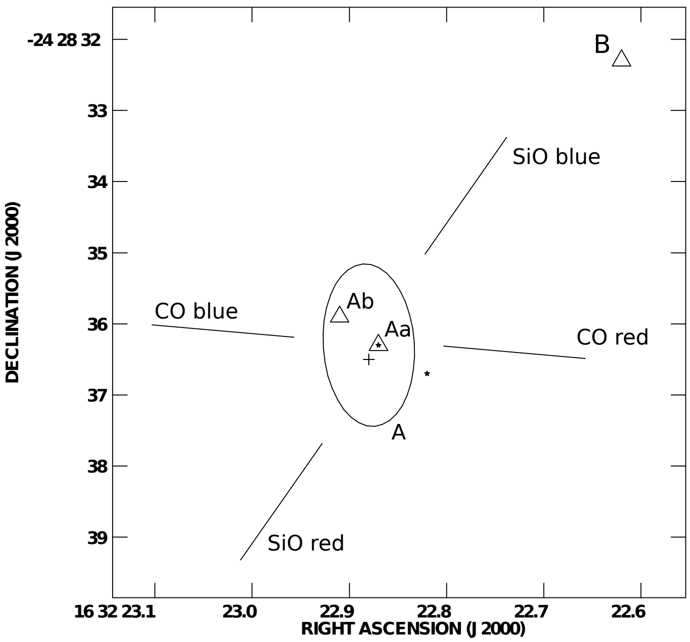

Fig. 2. Scheme of the distribution of dust and molecular material in I16293. The plus signal indicates the position of the peak intensity of our VLA water maser data. The ellipse is the deconvolved size of the dust continuum source A as derived by Rao et al. (2009). Triangles denote the position of the submillimeter condensations observed by Chandler et al. (2005). Stars denote the VLBI water maser detections of Imai et al. (2007) and straight lines denotes the direction of the CO and SiO outflows associated with this core (Rao et al. 2009).

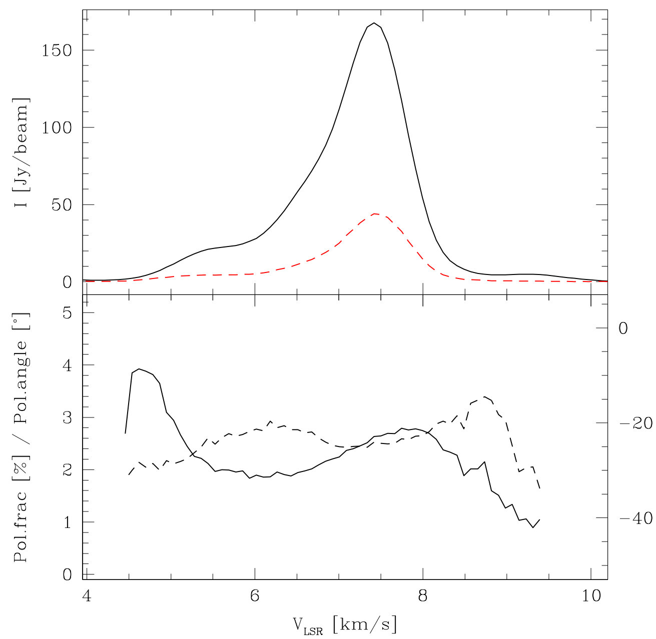

Fig. 3. Stokes I (black line) and linear polarization intensity (multiplied by a factor of 10, red dashed line) spectra of the water maser emission (upper panel). The spectra of polarization fraction (black line, left scale) and position angle (dashed line, right scale) are also shown (lower panel).

brightest component. The remaining maser features show only residual Zeeman profiles with amplitudes at the rms level.

4. H_2O masers and the SiO/CO outflows

Fig. 6 shows that the three possible maser features unresolved in our data are distributed linearly. The velocity shift observed between $V_{LSR} \simeq 5.7$ km s^{-1} and higher velocities is oriented in a E–W direction (PA $\simeq$ 110°). The proximity with source *Aa* and the complex outflow configuration observed in this zone suggest that the maser emission is being pumped in the dense circumstellar material around this object.

Rao et al. (2009) report a strong and very young SiO outflow extending toward the northwest-southeast (NW–SE) direction, with the SE lobe detected at redshifted LSR velocities (see Fig. 2). This SE component is also traced by a CO (3-2) outflow at $V_{LSR} \simeq 9$ km s^{-1} (Fig. 7 in Rao et al. 2009). The CO outflow has a dominant E–W orientation and has already been reported in the literature (Yeh et al. 2008). Rao et al. (2009) claim that the SiO and CO outflows are centered on sources *Ab* and *Aa*, respectively. Nevertheless, it is hard to disentangle the powering sources from their molecules maps, since that the separation between *Aa* and *Ab* ($\sim 0.6''$) is much smaller than the HPBW of their SiO and CO maps ($\sim 3''$).

Our maser features are also detected at redshifted velocities and lie in a similar direction as the CO outflow. On the other hand, their positions south of *Aa* suggest that they may be excited by the SiO outflow. In fact, the SE lobes observed for both SiO and CO at redshifted velocities (Fig. 6 and 7 from Rao et al. 2009) match quite well to the LSR of our highest velocity features ($V_{LSR} \sim 9$ km s^{-1}). In addition, VLA 3.7 cm data from Chandler et al. (2005) show two sources, A1 and A2, close to *Aa* (see Fig. 6). These authors refer to A2 as a protostar which powers a radio jet due to the bipolar shape seen in their high-resolution maps. On the other hand, source A1 would be an ionized region produced by shocks between this flow and nearby dense gas. Therefore, it is possible that the water masers are generated in the interaction regions traced by the radio sources and the outflows.

Water masers detections were also reported toward source A through very long baseline (VLBI) observations (Imai et al. 2007). The milliarcsecond resolution data revealed a spot exactly over *Aa* and another one to the SW of it (see Fig. 2). While the former may have been excited in the circumstellar gas of source *Aa*, the latter is likely created by shocks in the E–W outflow. The redshifted lobe of this emission has an open shell structure, therefore masers off from the outflow main axis are expected.

5. The line-of-sight magnetic field strength in I16293

From the Zeeman splitting formalism, the magnetic field strength can be correlated to the fraction of circular polarization by (see, for instance, Fiebig & Guesten 1989)

$$P_V = (V_{max} - V_{min})/I_{max} \quad (1)$$
$$= 2 \times A_{F-F'} \times (B\cos\theta)/\Delta V_I, \quad (2)$$

where the $A_{F-F'}$ coefficient depends on the maser rotational levels F and F', the intrinsic thermal linewidth Δv_{th} and the maser saturation degree, while Δv_I is the *FWHM* of the total power spectrum. For the $A_{F-F'}$ coefficient, we adopted the range of 0.012 to 0.018, since these values are consistent with models and observations (Nedoluha & Watson 1992; Vlemmings et al. 2002). The water maser spectrum is a blend of different velocity components, so we adopt a linewidth ranging from 0.75 km s^{-1}, a typical value found in other regions (Vlemmings et al. 2006), to 1.0 km s^{-1}, the maximum estimated value in I16293 from our

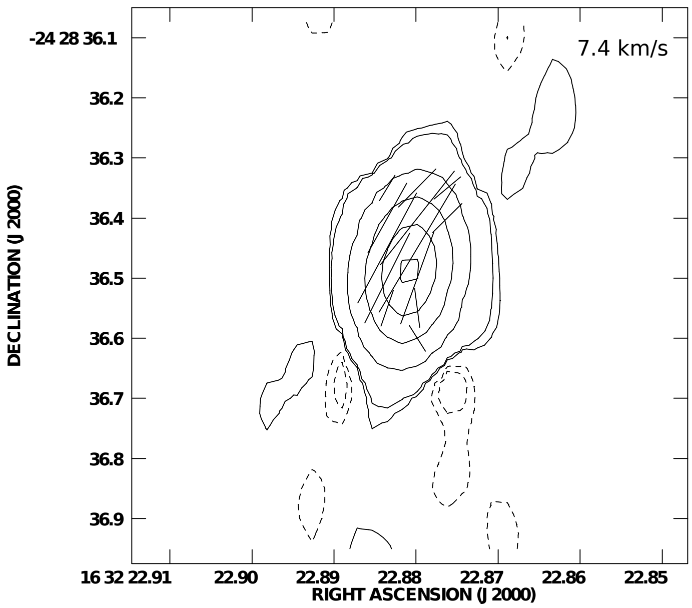

Fig. 4. Distribution of H_2O linear polarization vectors in the brightest emission channel ($V_{LSR} \simeq 7.4$ km s^{-1}). Contours are -50, -30, 30, 50, 500, 3×10^3, 1×10^4, $2 \times 10^4 \times 8$ mJy beam^{-1}. Only polarization vectors whose $P > 1\%$ are plotted. Vectors are sampled as 1/2 of a beam.

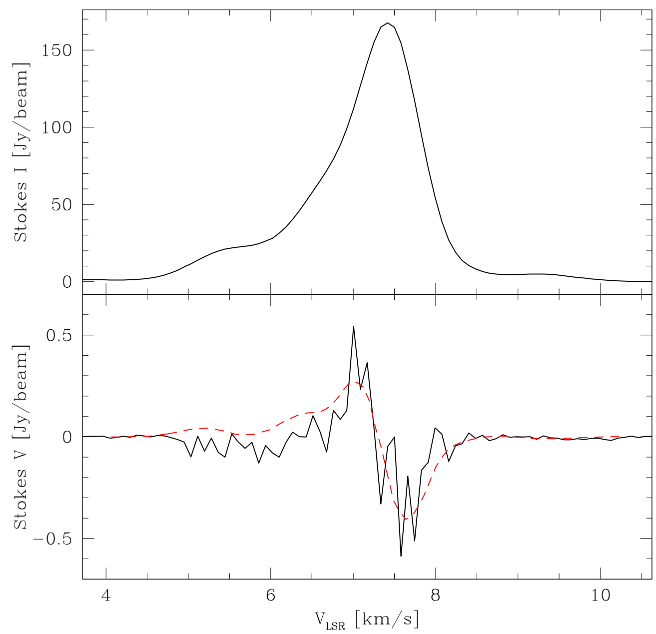

Fig. 5. Stokes I (upper panel) and Stokes V (lower panel) spectra of the water maser emission. The red dashed line is the scaled derivative of total power I in order to guide the eye.

spectral profile. For these values, we find that B_{LOS} ranges from ~ -94 to ~ -188 mG. The negative signal is inferred from the Stokes V shape, meaning that the field is pointing toward the observer. For narrower linewidths (~ 0.75 km s^{-1}), which is more realistic for resolved water maser lines, the field strength ranges from ~ -94 to ~ -141 mG (see Table 2). We note, however, that given that the linear polarization fraction is about 3%, this maser is likely unsaturated and the field strength determination is a fair approximation.

Fig. 4 shows the linear polarization vectors at the velocity channel with the brightest emission. There is a degeneracy between the position angle of the linear polarization vectors and the magnetic field direction projected in the plane-of-sky (POS). The position angle of the polarization will be parallel or perpendicular to the magnetic field in the POS for $\theta > \theta_{crit}$ or $\theta < \theta_{crit} = 55°$, respectively (Goldreich et al. 1973), where θ is the angle between B and the maser propagation direction and θ_{crit} is the so called Van Vleck angle. Given that the linear polarization fraction P_l depends on θ and the maser saturation level, we could in principle constrain the value of θ from our data and solve for this ambiguity. We used a non-LTE radiative transfer model in order to fit the observed intensity I and polarization fraction P_l. However, since our line is a blend of features spatially unresolved, we were unable to determine θ. Although observations at more extended configurations are needed to achieve this goal, we can at least claim that the POS field topology is quite ordered in both cases, i. e., it would remain ordered if rotated by 90°.

According to the submm data of Rao et al. (2009), the direction of the dust polarization vectors associated with source A averages to 95°, which implies that the POS magnetic field lines have a PA of 5° with respect to the North direction. Assuming that the 22 GHz polarization vectors in Fig. 4 are parallel to the POS magnetic field, the main direction of the field lines is $-23°$ (or its supplement, 157°) with respect to the North direction, as reported in Section 3.2. On the other hand, if our polarization vectors are perpendicular to the POS field, their main direction would then be 67°. Although two distinct scales are being compared, it is interesting to point out that in both cases there is clearly a change in the direction of the field lines in the small scales traced by our VLA data. In the case of parallel field lines and polarization vectors, such a change could be produced by the interaction of the SiO outflow and the magnetic field, given that the field lines lie almost in the same direction of the outflow (PA $\sim$ 145°, Fig. 2).

6. Preshock magnetic fields and post-shock densities

The only previous estimation of the magnetic field strength toward I16293 was performed by Claussen et al. (2003), who used VLBI observations of water masers to estimate $B_{LOS} \sim -40$ mG. Their maser spots appear associated with the A1 cm source (Fig. 6), with a projected separation of ~ 20 AU at $V_{LSR} \sim 2.5$ km s^{-1}(Claussen, private communication). Since this LSR velocity is similar to the core ambient velocity, it is unlike that this emission traces the same region observed with our VLA data. In any case, our work is then one of the first determinations of the field strength in a low-mass young stellar object at densities larger than 10^8 cm^{-3}. As discussed in § 4, the observed maser emission is excited in zones of compressed gas produced by shocks between the outflows and the ambient gas. In an ionized medium, shocks compress the gas by a factor m_A, the Alfvénic Mach number defined as v_s/v_A, where v_s is the shock velocity and v_A the Alfvén speed. The magnetic field B_0 in the pre-shock zone is also enhanced by a factor m_A in the shocked gas so that $B_s \sim m_A \times B_0$. Since v_A varies with $B_0(n)^{-1/2}$, then B_s is proportional to $v_s(n)^{1/2}$, where n is the volume density of the pre-shock region. Rearranging this expression, the pre-shock density can be written as (Kaufman & Neufeld 1996):

$$n_0 = 1.6 \times 10^6 \left(\frac{B_s}{\mathrm{mG}}\right)^2 \left(\frac{v_s}{\mathrm{km\ s^{-1}}}\right)^{-2} \mathrm{cm}^{-3}. \tag{3}$$

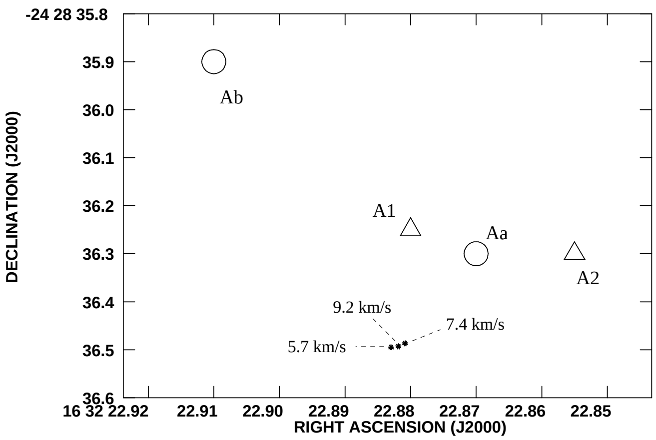

Fig. 6. Possible independent maser features (stars) as derived by gaussian fits. The accuracy in the position of each maser feature is ∼ 2 mas, while the positions of the submm and cm sources are accurate within ∼ 25 mas and ∼ 10 mas, respectively. The numeric labels are the maser velocities with respect to the Local Standard of Rest (LSR). The 3.7 cm sources A1 and A2 (triangles) and the submm sources *Aa* and *Ab* (circles) are also shown (Chandler et al. 2005). The sizes of each symbol are not proportional to their deconvolved sizes or their intensities.

Table 2. *B*-field strength calculation from Eq. 2 (assuming $\Delta V_I = 0.75$ km s^{-1})

	$A_{F-F'} = 0.012$	$A_{F-F'} = 0.015$	$A_{F-F'} = 0.018$
$B_{\rm LOS}$ (mG)	−141	−113	−94

The LOS magnetic field strength calculated in § 5 can be rescaled in order to obtain the total field strength $B_{tot} = B_s$ in the shocked zone. According to Crutcher et al. (1999), the squared LOS magnetic field $\langle B_{\rm LOS}\rangle^2$ averaged over several lines of sight in the Galaxy is $\sim B^2_{\rm tot}/3$. The shock velocities are retrieved from submm water emission detected in shocked zones around I16293 (Ristorcelli et al. 2005). These data were modeled as C-shocks (low velocity, non-dissociative shocks, Kaufman & Neufeld 1996) with shock velocities between 12 – 15 km s^{-1}. Applying those values to equation 3, we obtain pre-shock densities of $\sim 4.2^{+2.3}_{-2.4} \times 10^8$ cm^{-3}, which is consistent with the typical densities where water masers are eventually pumped. The upper/lower limits in the number density refer to the B_s determinations for the two limit $A_{F-F'}$ cases (Table 2).

If the magnetic field plays a dominant role over the outflow dynamics, the magnetic pressure should be similar to the shock ram pressure, i. e.,

$$B_s^2/8\pi = \rho_0 v_s, \quad (4)$$

where ρ_0 is the pre-shock density. For the field strength B_s determined in the previous section and shock velocities of Ristorcelli et al. (2005), we find a mean pre-shock density of $\sim 5.1 \times 10^8$ cm^{-3}, which is consistent with the pre-shock densities calculated from equation 3 and in line with a magnetically controlled outflow evolution.

Assuming magnetic flux-freezing, the compression of an ordered magnetic field (B_0) amplifies the field strength in proportion to the gas density as follows

$$\frac{B_0}{n_0} = \frac{B_s}{n_s} \quad (5)$$

where n_s is the post-shock density. If we consider that the shock compresses the well established field geometry in the submm maps of Rao et al. (2009), which predict a (scaled) $B_0 \simeq 9$ mG at densities $n_0 \simeq 4.9 \times 10^7$ cm^{-3}, and using the post-shock field intensity B_s calculated from our data, we find post-shock densities of $\sim 1.3 \times 10^9$ cm^{-3}, which is expected for effective water maser pumping. In a more conservative approach, we rescale the magnetic field strength of Rao et al. (2009) using $B \propto n^\kappa$, where κ may assume distinct vales depending on the dynamics of the core: $\kappa = 0.5$ for a cloud evolution controlled by the magnetic field (Crutcher et al. 1999), $\kappa = 0.47$, magnetic evolution as modeled by Fiedler & Mouschovias (1993) and $\kappa = 0.67$, for a free-fall cloud collapse. For the three cases, the pre-shock magnetic field in the calculated pre-shock densities ranges between ∼ 24 and 36 mG. Applying again equation 5, we obtain post-shock densities ranging between $\sim 2 - 5 \times 10^9$ cm^{-3}, again consistent with typical H_2O maser densities, but unable to discern in which dynamical regime, if magnetic or turbulent, the core evolves.

The H_2O maser emission of I16293 is strong (> 200 Jy) and stable over a few weeks but highly variable over months, as shown by surveys performed toward this source (Wilking & Claussen 1987; Claussen et al. 1996; Furuya et al. 2003). We are then encouraged to carry out VLBI observations in the future. With these observations, the blended maser components found in this work will be likely resolved both spatially and spectroscopically. We will then be able to apply radiative transfer models such as in Vlemmings (2006) to derive the full 3-D magnetic field properties as already done in other star-forming regions (e. g., Cepheus A HW2, Vlemmings et al. 2006).

7. Conclusions

This work reports on the H_2O ($6_{16} - 5_{23}$) maser emission observed with the VLA/EVLA toward the low-mass source IRAS 16293-2422. This is one of the first estimations of the line-of-sight magnetic field strength in a low-mass protostar at densities larger than 10^8 cm^{-3}. From this study, we obtained insights on the dynamics of this object at such high densities. Our main conclusions are:

– We detect strong water maser emission associated with the submm source *Aa*.
– The maser spectrum has a non-Gaussian profile, indicating the presence of at least three maser features covering a velocity range of ∼ 3.5 km s^{-1} distributed in a linear configuration. Those components are likely excited in zones of compressed gas produced by shocks in the outflow activity of I16293.
– The obtained Stokes V spectrum is consistent with Zeeman emission. The mean LOS magnetic field strength is ∼ 113 mG. The POS field topology retrieved from the linear polarimetry shows an ordered pattern consistent with larger scales field morphologies.
– The post- and pre-shock densities calculated from our field strength estimation are consistent with the typical densities expected for H_2O maser pumping.
– The dynamics of the outflow evolution in these sources are likely regulated by the magnetic field, since that the magnetic pressure in the shocked gas is similar to the pre-shock ram pressure.

Acknowledgements. The authors would like to thank the anonymous referee for a constructive report that helped to improve the paper. We are also grateful to Gabriele Surcis for running the radiative transfer models on the maser data. This research was partially supported by the Deutsche Forschungsgemeinschaft (DFG) through the Emmy Noether Research grant VL 61/3-1 and through SFB

956. FOA, JMG and JMT also acknowledge support from MICINN (Spain) AYA2011-30228-C03 and AGAUR (Catalonia) 2009SGR1172 grants.

References

Bisschop, S. E., Jørgensen, J. K., Bourke, T. L., Bottinelli, S., & van Dishoeck, E. F. 2008, A&A, 488, 959
Briggs, D. 1995, PhD thesis, The New Mexico Institute of Mining and Technology
Ceccarelli, C., Loinard, L., Castets, A., Tielens, A. G. G. M., & Caux, E. 2000, A&A, 357, L9
Chandler, C. J., Brogan, C. L., Shirley, Y. L., & Loinard, L. 2005, ApJ, 632, 371
Claussen, M., Sarma, A. P., Wootten, A., Marvel, K. B., & Wilking, B. 2003, in Bulletin of the American Astronomical Society, Vol. 35, American Astronomical Society Meeting Abstracts, 1362
Claussen, M. J., Wilking, B. A., Benson, P. J., et al. 1996, ApJS, 106, 111
Crutcher, R. M., Roberts, D. A., Troland, T. H., & Goss, W. M. 1999, ApJ, 515, 275
Elitzur, M., Hollenbach, D. J., & McKee, C. F. 1989, ApJ, 346, 983
Fiebig, D. & Guesten, R. 1989, A&A, 214, 333
Fiedler, R. A. & Mouschovias, T. C. 1993, ApJ, 415, 680
Furuya, R. S., Kitamura, Y., Wootten, A., Claussen, M. J., & Kawabe, R. 2003, ApJS, 144, 71
Goldreich, P., Keeley, D. A., & Kwan, J. Y. 1973, ApJ, 179, 111
Goodman, A. A., Jones, T. J., Lada, E. A., & Myers, P. C. 1992, ApJ, 399, 108
Goodman, A. A., Jones, T. J., Lada, E. A., & Myers, P. C. 1995, ApJ, 448, 748
Imai, H., Nakashima, K., Bushimata, T., et al. 2007, PASJ, 59, 1107
Jørgensen, J. K., Bourke, T. L., Nguyen Luong, Q., & Takakuwa, S. 2011, A&A, 534, A100
Kaufman, M. J. & Neufeld, D. A. 1996, ApJ, 456, 250
Kuan, Y., Huang, H., Charnley, S. B., et al. 2004, ApJ, 616, L27
Lazarian, A., Goodman, A. A., & Myers, P. C. 1997, ApJ, 490, 273
Loinard, L., Torres, R. M., Mioduszewski, A. J., & Rodríguez, L. F. 2008, ApJ, 675, L29
Looney, L. W., Mundy, L. G., & Welch, W. J. 2000, ApJ, 529, 477
Mundy, L. G., Wootten, H. A., & Wilking, B. A. 1990, ApJ, 352, 159
Nedoluha, G. E. & Watson, W. D. 1992, ApJ, 384, 185
Pérez-Sánchez, A. F., Vlemmings, W. H. T., & Chapman, J. M. 2011, MNRAS, 418, 1402
Rao, R., Girart, J. M., Marrone, D. P., Lai, S., & Schnee, S. 2009, ApJ, 707, 921
Ristorcelli, I., Falgarone, E., Schöier, F., et al. 2005, in IAU Symposium, Vol. 235, IAU Symposium, 227P
Sanna, A., Moscadelli, L., Cesaroni, R., et al. 2010a, A&A, 517, 71
Sanna, A., Moscadelli, L., Cesaroni, R., et al. 2010b, A&A, 517, 78
Sarma, A. P., Troland, T. H., & Romney, J. D. 2001, ApJ, 554, L217
Stark, R., Sandell, G., Beck, S. C., et al. 2004, ApJ, 608, 341
Surcis, G., Vlemmings, W. H. T., Curiel, S., et al. 2011a, A&A, 527, 48
Surcis, G., Vlemmings, W. H. T., Torres, R. M., van Langevelde, H. J., & Hutawarakorn Kramer, B. 2011b, A&A, 533, 47
Tamura, M., Hayashi, S. S., Yamashita, T., Duncan, W. D., & Hough, J. H. 1993, ApJ, 404, L21
Terebey, S., Vogel, S. N., & Myers, P. C. 1992, ApJ, 390, 181
Vlemmings, W. H. T. 2006, A&A, 445, 1031
Vlemmings, W. H. T. 2008, A&A, 484, 773
Vlemmings, W. H. T., Diamond, P. J., & van Langevelde, H. J. 2002, A&A, 394, 589
Vlemmings, W. H. T., Diamond, P. J., van Langevelde, H. J., & Torrelles, J. M. 2006, A&A, 448, 597
Walker, C. K., Lada, C. J., Young, E. T., & Margulis, M. 1988, ApJ, 332, 335
Wardle, J. F. C. & Kronberg, P. P. 1974, ApJ, 194, 249
Wilking, B. A. & Claussen, M. J. 1987, ApJ, 320, L133
Wootten, A. 1989, ApJ, 337, 858
Yeh, S. C. C., Hirano, N., Bourke, T. L., et al. 2008, ApJ, 675, 454